

RESONANT ELASTIC SHAFT THRUST VECTORING: IMPLICATIONS FOR UAV DESIGNS

Haofei Guan[1] & KC Wong[1]

[1]The University of Sydney (USYD), Sydney, NSW, Australia

Abstract

This paper tests the bounded feasibility of a Resonant Elastic Shaft (RES) as the primary control effector of a fixed-wing UAV. RES is a monolithic compliant shaft whose geometry and stiffness distribution convert cyclic motor-torque modulation into coupled bending-torsion deformation at the propeller. Four linked criteria are examined: vector generation, aircraft-level control authority, physical integration, and controlled flight. At a cruise-like mechanism condition, optical estimation gives a vector half-angle of $10^\circ \pm 1^\circ$ with full azimuthal phase coverage. The flown demonstrator has a measured mass of $109.8\,\mathrm{g}$, centre of gravity $95\,\mathrm{mm}$ aft of the root leading edge, and propeller vector arm of $162 \pm 1\,\mathrm{mm}$. For an assumed $C_L = 0.5$–0.6, an analytical small-disturbance calculation gives a 5° pitch restoring moment of 0.0045–$0.0054\,\mathrm{N\,m}$ and a balancing thrust requirement of 0.160–$0.192\,\mathrm{N}$ at the nominal vector angle. The RES was integrated as one centreline propulsion/control assembly without wing-mounted actuators. Three recordings from two flights show launch, sustained forward flight, straight flight, and turning; the longer recorded flight is approximately $3\,\mathrm{min}$. These results establish proof-of-concept feasibility, not full characterization. Control bandwidth, calibrated flight dynamics, structural life, efficiency, cost, and matched-baseline performance remain unmeasured.

Keywords: thrust vectoring; compliant mechanisms; fixed-wing UAV; propulsion-led attitude control; modular design

1. Introduction

This paper asks a limited design question: can a single compliant vectored propulsor generate a usable vector, provide plausible aircraft-level moment authority, be integrated into a light fixed-wing airframe, and support controlled flight without wing-mounted actuators? The subject is the Resonant Elastic Shaft (RES), a monolithic compliant shaft in which cyclic motor-torque modulation produces coupled bending-torsion deformation and redirects the propeller axis. The study is a bounded feasibility test, not a complete characterization or an optimization.

1.1 Literature basis and technical gap

Five literature areas delimit the contribution. Each source-supported statement is separated from the interpretation applied to RES.

Morphing structures. A broad review of structural shape-changing concepts for fixed- and rotary-wing aircraft reports that relatively few concepts had progressed to wind-tunnel or flight testing [1]. A later review organizes morphing-aircraft research around configuration design, modelling, and control [2]. RES uses continuous deformation in a propulsion member, but it is not presented as a morphing wing or as evidence of aerodynamic benefit.

Compliant mechanisms. The Mission Adaptive Compliant Wing programme reported design, performance, and flight-test results for a continuous compliant wing [3]. A variable-camber wing demonstrator was fabricated with large-deformation compliant leading and trailing edges [4]. RES similarly embeds motion in a continuous member, but its load capacity, fatigue life, and benefit relative to hinged hardware have not been compared.

Flexible-shaft dynamics. An elastodynamic model has been derived that couples bending and torsion of a rotating shaft [5]. Coupling among reference rotation, shaft torsion, and blade bending has also been modelled [6]. These studies provide dynamic analogies for RES; the present flexible model uses provisional effective properties and is not yet predictive.

Distributed propulsion. The NASA SCEPTOR demonstrator uses 12 high-lift propellers and two cruise propellers; its design study reports a $2.5\times$ reduction in wing area relative to the baseline aircraft [7]. Aircraft concepts based on distributed electrically driven propulsors have been reviewed [8]. An aero-propulsive study found that individual pusher-propeller efficiency varied with propeller location and thrust level [9]. RES is not distributed propulsion. The relevant design principle is that propulsor placement, airframe sizing, and control architecture should be considered jointly.

Modern UAV thrust vectoring. An overactuated quadrotor with tilting propellers has been modelled and experimentally validated [10]. Flight control for a quad tilt-rotor UAV has been demonstrated over large attitude changes, including flight at a 90° pitch attitude [11]. Trajectory-tracking control has been proposed for UAVs with limited thrust-vectoring capability [12]. RES instead examines one centreline propeller without a servo tilt joint; passive fixed-wing coupling supplies the remaining lateral response. These fields motivate, but do not validate, RES. The technical gap is the system-level connection between distributed compliant shaft deformation and a fixed-wing control architecture. The contribution is therefore organized as four linked feasibility criteria: Criterion 1, vector generation; Criterion 2, aircraft-level authority; Criterion 3, physical integration; and Criterion 4, controlled flight. Each criterion uses a different evidence type, and no simulation, calculation, or video is asked to validate the complete system alone.

1.2 Evidence classes and claim boundary

Direct measurements are reported with units and uncertainty where available. Video observations are labelled as optical estimates or observed states. Aerodynamic and control-moment values are analytical estimates with their assumptions stated. Flexible-body and RealFlight outputs are model quantities only; RealFlight is not treated as physical validation until its aerodynamic derivatives and RES dynamics are calibrated. The strongest admissible conclusion is proof-of-concept feasibility. Efficiency, bandwidth, structural life, manufacturing cost, and superiority over a matched conventional aircraft remain outside the present evidence.

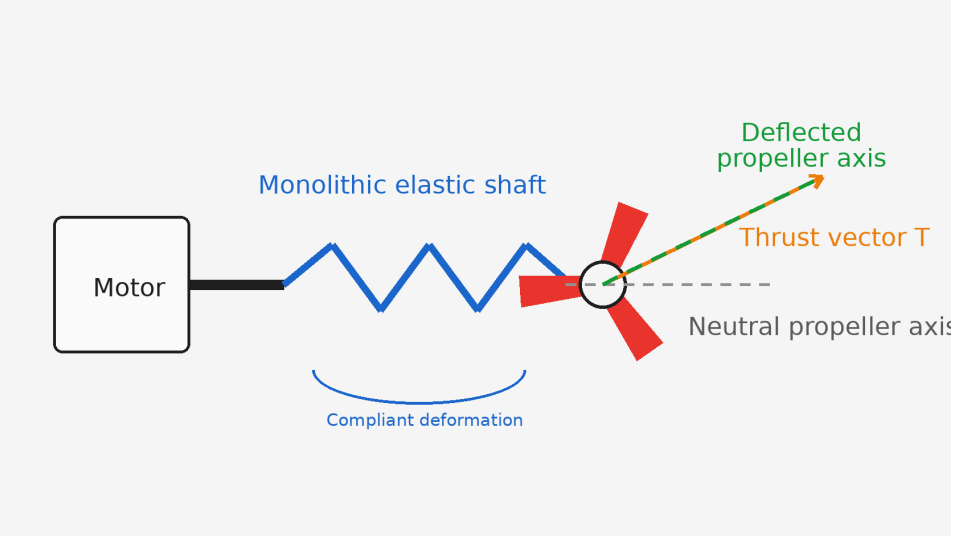
Section 2 defines the mechanism and model quantities. Section 3 fixes the four feasibility criteria and the reference condition. Sections 4–7 evaluate Criteria 1–4. Section 8 audits the evidence and defines the next measurements.

2. RES actuation and model quantities

2.1 Deformation principle

The motor-side and propeller-side axes are connected by a monolithic elastic shaft rather than an articulated gimbal, hinge-defined hub, or swashplate transmission. Periodic input torque is transmitted through the shaft and produces a coupled bending-torsion response. The shaft deformation reorients the propeller axis and hence the thrust vector.

Figure 1 gives the motor–shaft–propeller interpretation and the current prototype. The elastic shaft is both the load path and the vectoring element.



(a) Conceptual RES sketch.



(b) Current RES prototype photograph.

Figure 1 – Overall RES concept used in this paper. The sketch gives the mechanism interpretation, and the photograph shows the current physical implementation in the same general layout.

The neutral and deflected views in Fig. 2 are summarized by

$$\Delta\gamma = -\left(\frac{\theta}{k}\right)\cos\left(\gamma_I + P\right) \tag{1}$$

where $\Delta\gamma$ is shaft-angle change, θ is the drive-side angular input quantity, k is a lumped elastic scaling coefficient, γ_I is the initial working angle, and P is a phase-like offset. Equation (1) preserves the phase-dependent deformation description; it is not a calibrated transfer function or complete structural model. Coupled bending–torsion of a rotating shaft provides one relevant modelling basis [5]. Coupled shaft-torsion and blade-bending dynamics provide another [6]. Criterion 1 below instead uses the observed output-vector envelope.

2.2 Flexible-body substitution

The motor, propeller-aerodynamic, torque-modulation, and vector-reconstruction framework follows [20]. Only the former concentrated spherical-joint mechanism is replaced. Figure 3 uses a $10\,\mathrm{mm}$ cylindrical beam in parallel with a $10\sqrt{2}\,\mathrm{mm}$ rectangular branch, $\pm 45^\circ$ branch rotations, and $5\,\mathrm{mm}$ lateral offsets. Initial effective TPU 95A inputs are $\rho = 1200\,\mathrm{kg\,m^{-3}}$, $E = 40\,\mathrm{MPa}$, $\nu = 0.48$, and modal damping ratio $\zeta = 0.10$. These are model assumptions requiring experimental calibration, not measured specimen properties.

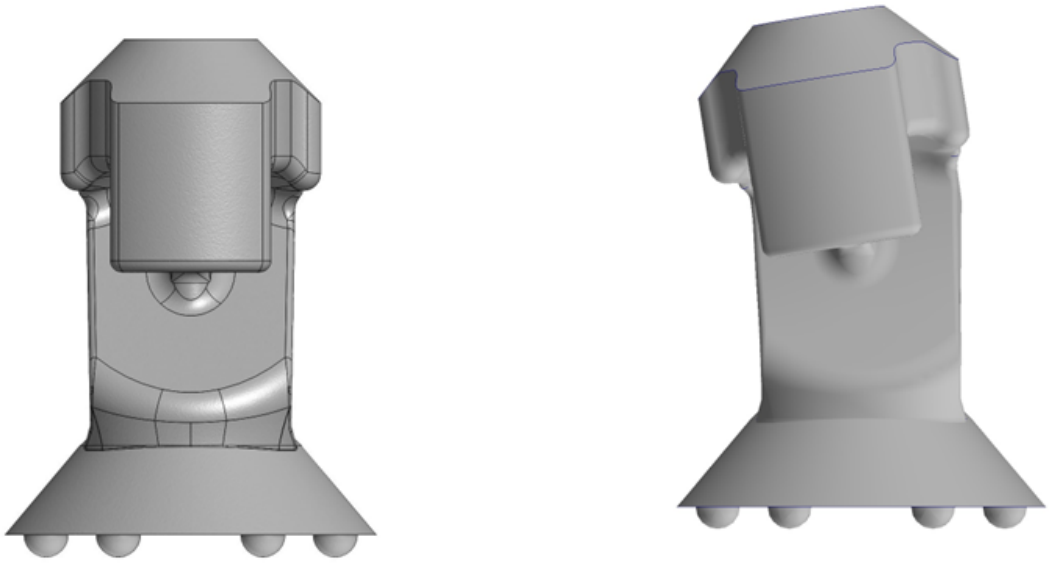
The model change is topological as well as parametric: motion is distributed over two compliant paths rather than concentrated at a passive joint.

2.3 Platform-frame reconstruction and scope result

Figure 4 shows the final flexible-body assembly used for the illustrative vectoring run. The image establishes the implemented body arrangement and the relative orientation of its body frames; it is not used to measure deformation.

Two related outputs must be distinguished. First, let B denote the neutral motor-side frame and F the propeller-side follower frame. The Transform Sensor rotation matrix $\mathbf{R}_{BF}(t)$ maps F-resolved components into B. With local propeller axis $\mathbf{e}_0 = [0,0,1]^T$, the geometric rotor-axis direction is

$$\mathbf{n}^B(t) = \mathbf{R}_{BF}(t)\mathbf{e}_0, \qquad \delta(t) = \cos^{-1}\left(\mathbf{e}_0^T\mathbf{n}^B(t)\right), \qquad \chi(t) = \mathrm{atan2}\left(n_y^B, n_x^B\right). \tag{2}$$



(a) Neutral geometry. (b) Deflected output axis.

Figure 2 – RES deformation views. The elastic member provides the core function by changing the output-side propeller axis relative to the input-side axis.

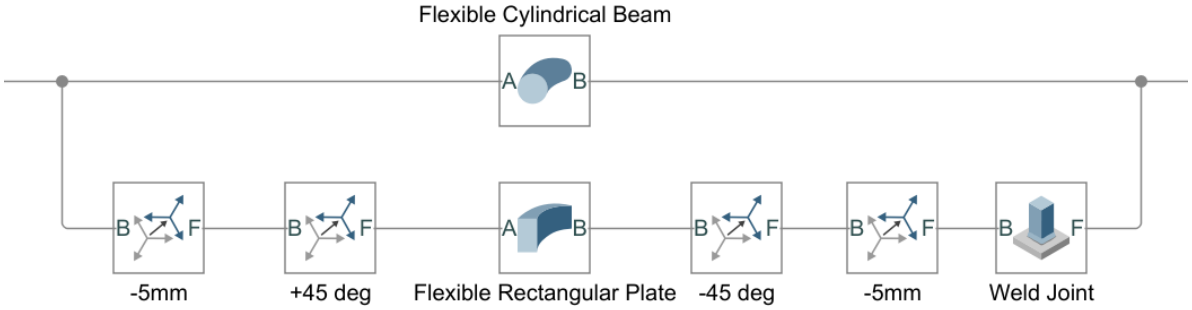


Figure 3 – Modification to the previously published rotor simulation model [20]: the idealized joint mechanism is replaced by parallel flexible cylindrical and rectangular beam paths.

Here δ is vector half-angle and χ is azimuth about the neutral axis. The corresponding control-moment magnitude is $M_{TV}(t) = T(t) l \sin\delta(t)$.

Second, the available scope records angular velocity rather than $\mathbf{n}^B$. Let W and P denote the world and platform frames. The Transform Sensor returns $\omega^W = [\omega_x^W, \omega_y^W, \omega_z^W]^T$ in $\mathrm{rad\,s^{-1}}$. If $\mathbf{e}_{P,i}^W$ is platform-axis i resolved in W, each platform component is the scalar projection

$$\omega_i^P(t) = \left(\mathbf{e}_{P,i}^W(t)\right)^T \omega^W(t), \qquad i \in \{x,y,z\}. \tag{3}$$

Stacking the three projections gives $\omega^P = \mathbf{R}_{PW}\,\omega^W$, where the rows of $\mathbf{R}_{PW}$ are the transposed platform basis vectors. This calculation is stated directly because a block diagram would add only the three products and sums in Eq. (3).

One $8\,\mathrm{s}$ transient run is presented as an illustrative consistency case for this particular model and input schedule. Modulation depth is zero before $t = 2\,\mathrm{s}$; thereafter the positive-only cyclic torque command is bounded by $0 \le \tau(t) \le 2\bar{\tau}$ while its mean remains $\bar{\tau}$. The resulting platform-frame components depart from the near-neutral start-up response after $t = 2\,\mathrm{s}$ and reach a bounded periodic regime by approximately $t = 4\,\mathrm{s}$ (Fig. 5). Screen digitization of the plotted $t = 4$–$8\,\mathrm{s}$ interval gives

$$\overline{\omega}^P \approx [-59,\ 25,\ 294]^T\,\mathrm{rad\,s^{-1}}, \quad \left\|\overline{\omega}^P\right\| \approx 301\,\mathrm{rad\,s^{-1}}\ (2.87\times10^3\,\mathrm{rpm}). \tag{4}$$

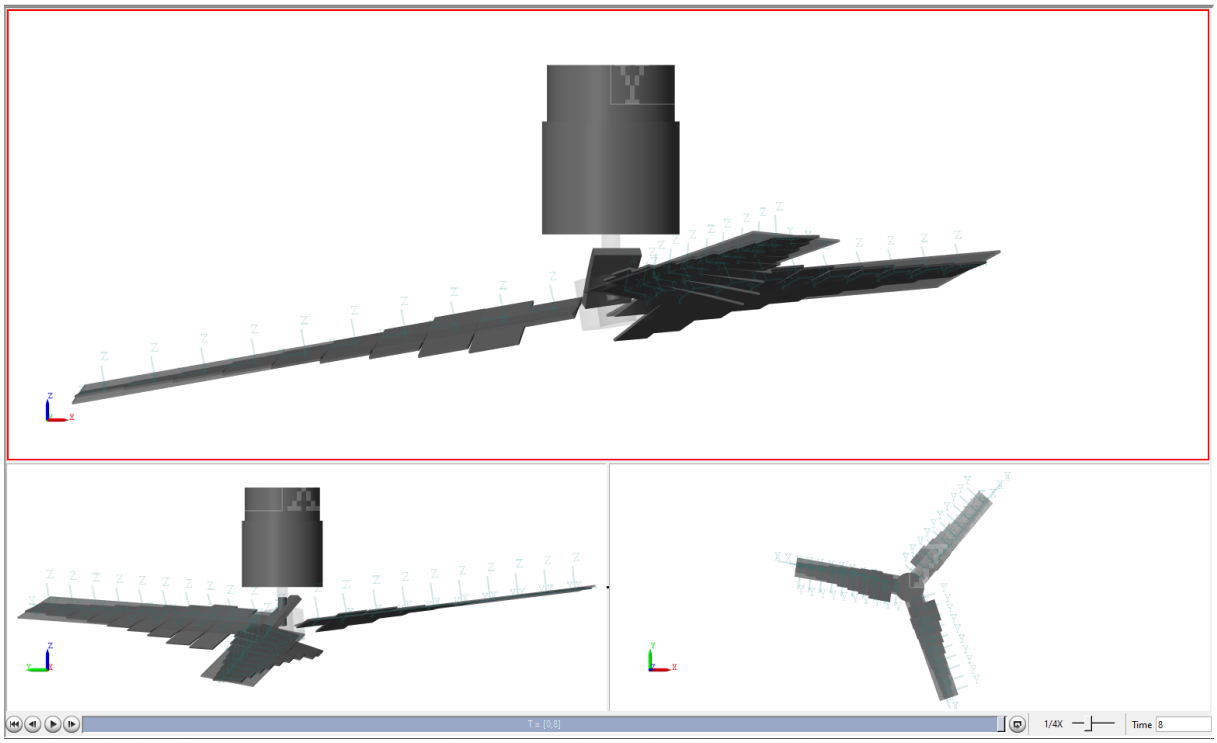


Figure 4 – Final flexible-body assembly used in the illustrative vectoring run, shown in one oblique and two orthogonal views. The light-blue markers identify body frames within the model. The image is included to show the implemented simulated bodies; displayed deformation is not interpreted as a dimensional measurement.

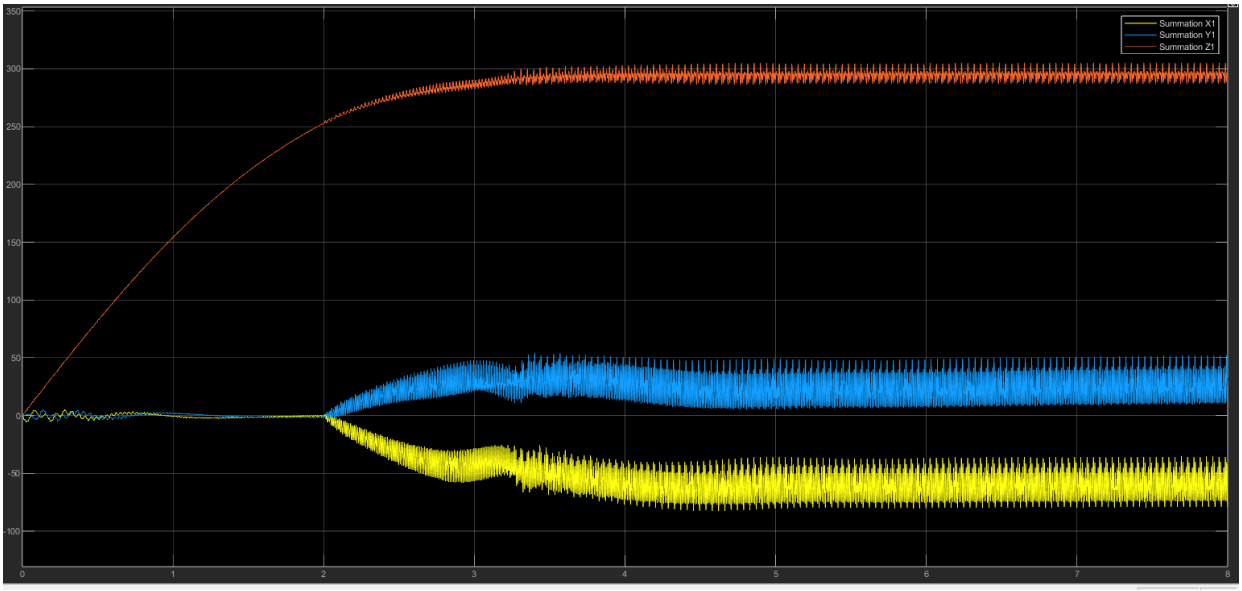


Figure 5 – Platform-frame angular-velocity scope for the $8\,\mathrm{s}$ flexible-body run: ω_x^P is yellow, ω_y^P blue, and ω_z^P orange. Torque-modulation depth changes at $t = 2\,\mathrm{s}$, and $t = 4$–$8\,\mathrm{s}$ is used for the settled screen-digitized result. The horizontal axis is simulation time in seconds; the vertical axis is angular velocity in $\mathrm{rad\,s^{-1}}$.

The direction of this mean is $\delta_\omega = \mathrm{atan2}\left(\sqrt{\bar{\omega}_x^2 + \bar{\omega}_y^2}, \bar{\omega}_z\right) \approx 12.3^\circ$ and $\chi_\omega = \mathrm{atan2}(\bar{\omega}_y, \bar{\omega}_x) \approx 157^\circ$. Across four consecutive $1\,\mathrm{s}$ windows, the screen-derived mean magnitude is 300.8–$301.1\,\mathrm{rad\,s^{-1}}$, δ_ω is 12.3°–12.5°, and χ_ω is 155°–158°. The visible settled component envelopes are approximately $-81 \le \omega_x^P \le -35$, $6 \le \omega_y^P \le 52$, and $286 \le \omega_z^P \le 304\,\mathrm{rad\,s^{-1}}$. The model therefore reaches a stable mean angular-velocity direction with a superposed periodic response, rather than a constant vector.

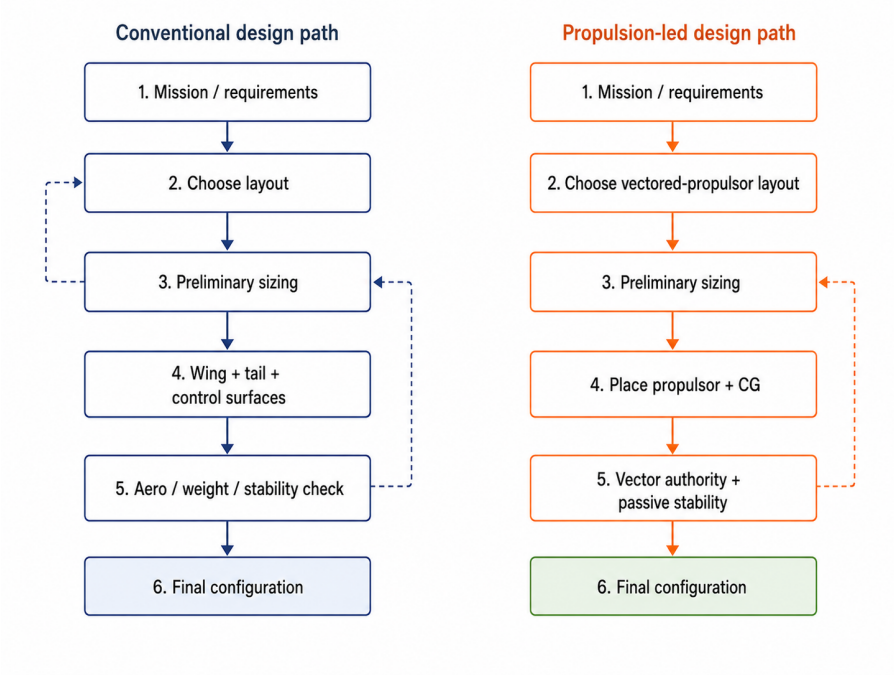


Figure 6 – Iterative conventional and propulsion-led design paths. The principal difference is the early treatment of the vectored propulsor as the primary control effector.

The distinction between Eqs. (2) and (4) is essential. In a flexible rotor, ω can include spin, precession, and nutation, so δ_ω is not automatically the geometric vector half-angle δ. The present scope result quantitatively shows how this particular simulation develops bounded model motion and a stable cycle-mean rotational-velocity direction; it does not establish a configuration-independent performance value, thrust-vector magnitude, model accuracy, or agreement with the physical RES. Those require exported $\mathbf{R}_{BF}(t)$ data and calibrated effective material properties. Visual deformation amplification is excluded from all numerical interpretation.
For the planned calibrated sweep, the torque-to-vector frequency-response quantity remains

$$G_{\delta\tau}(j\omega) = \frac{\widehat{\delta}(\omega)}{\widehat{\Delta\tau}(\omega)}. \tag{5}$$

A settled sinusoidal sweep is intended to report geometric vector half-angle, cone circularity, azimuth coverage, resonant frequency, phase lag, and M_{TV} [19]. The single transient in Fig. 5 does not identify $G_{\delta\tau}$ or provide a calibrated prediction.

3. Bounded feasibility method

Figure 6 changes the order of emphasis within an otherwise iterative conceptual-design process. The vector envelope is defined first; propulsor placement, centre of gravity, passive stability, and preliminary sizing are then reconciled with the available moment. Early control constraints can materially change the feasible configuration [13].
The four criteria are stated before the results so that qualitative flight evidence is not interpreted as full validation. The evidence and pass condition for each criterion are as follows.
Criterion 1: vector generation. The question is whether RES redirects the propeller axis. The evidence is an optical estimate from the mechanism video. The pass condition is a repeatable nonzero vector half-angle with controllable azimuth.
Criterion 2: aircraft-level authority. The question is whether the vector moment is compatible with a representative restoring moment. The evidence combines the measured vector arm, optical angle estimate, and assumption-explicit longitudinal calculation. The pass condition is $Tl\sin\delta$ equal to or greater than the estimated restoring moment for a 5° disturbance.
Criterion 3: physical integration. The question is whether the architecture can be physically integrated. The evidence comprises measured mass and geometry, a component inventory, and

photographs. The pass condition is one flown propulsion/control assembly with no wing-mounted actuators.

Criterion 4: controlled flight. The question is whether the integrated aircraft can sustain controlled flight. The evidence comprises three recordings from two flights. The pass condition is visible launch, sustained forward flight, straight flight, and turning.

The reference condition combines the measured $109.8\,\mathrm{g}$ airframe, measured $162 \pm 1\,\mathrm{mm}$ vector arm, observed approximately 70% trimmed throttle, and the $10^\circ \pm 1^\circ$ cruise-like mechanism estimate. These quantities were not logged synchronously; the condition is a traceable feasibility point, not an identified operating map. The present aircraft is one feasible design point, not an optimum.

4. Criterion 1: vector generation

The prior RES-family mechanism video shows repeatable output-axis redirection under driven operation [21]. Optical inspection gives a cruise-like vector half-angle of $10^\circ \pm 1^\circ$ and full 360° azimuthal phase coverage. Deflections approaching 15° were observed only at substantially higher throttle nearer the resonant response and are not used as the reference value.

Criterion 1 is therefore met at proof-of-concept level: the output axis is redirected through a repeatable non-zero cone. The evidence does not establish bandwidth, input-output phase lag, load sensitivity, efficiency, repeatability statistics, or fatigue life. Equation (5) defines how the geometric response will be extracted after the flexible model is calibrated.

5. Criterion 2: aircraft-level control authority

Low-Reynolds-number propeller–wing experiments show that a tractor propeller slipstream changes the local wing aerodynamic loading [14]. The present design therefore uses a pusher layout, keeping the wing upstream of the vectored wake. A separate aero-propulsive analysis found that pusher-propeller efficiency depends on propeller location and thrust level [9]; the present study does not quantify that effect or claim an efficiency advantage. The selected trapezoidal wing has $b = 0.60\,\mathrm{m}$, $c_r = 0.22\,\mathrm{m}$, $c_t = 0.10\,\mathrm{m}$, 25° leading-edge sweep, and 5° dihedral. Its derived quantities are

$$\begin{aligned} S &= b\frac{c_r + c_t}{2} = 0.096\,\mathrm{m}^2, \\ AR &= \frac{b^2}{S} = 3.75, \\ \bar{c} &= \frac{2}{3}c_r\frac{1+\lambda+\lambda^2}{1+\lambda} = 0.1675\,\mathrm{m}, \end{aligned} \tag{6}$$

where $\lambda = c_t/c_r = 0.455$. A preliminary estimate gives $C_{L_\alpha} \approx 3.6\,\mathrm{rad}^{-1}$ [18]. Taking $x_{NP} = 103\,\mathrm{mm}$ and the measured $x_{CG} = 95\,\mathrm{mm}$ gives

$$SM = \frac{x_{NP} - x_{CG}}{\bar{c}} = 0.0478, \tag{7}$$

or 4.78%. The neutral point remains an analytical estimate.

For the measured mass $m = 0.1098\,\mathrm{kg}$, level-flight balance with $C_L = 0.5$–0.6 and air density $\rho_a = 1.225\,\mathrm{kg\,m^{-3}}$ gives $V = 5.52$–$6.05\,\mathrm{m/s}$. Dynamic pressure is $q = \frac{1}{2}\rho_a V^2$. The estimate $C_{m_\alpha} \approx -SMC_{L_\alpha}$ gives $C_{m_\alpha} = -0.172\,\mathrm{rad}^{-1}$, so a representative 5° pitch disturbance gives

$$|M_{\mathrm{rest}}| \approx qS\bar{c}|C_{m_\alpha}|\Delta\alpha = 0.0045\text{–}0.0054\,\mathrm{N\,m}. \tag{8}$$

The measured vector arm is $l = 0.162 \pm 0.001\,\mathrm{m}$ and the optically estimated cruise-regime RES half-angle is $\delta = 10^\circ \pm 1^\circ$, so, at the nominal values,

$$M_{TV} = Tl\sin\delta \approx 0.02813T. \tag{9}$$

Balancing the estimated restoring moment requires $T = 0.160$–$0.192\,\mathrm{N}$. This defines the Criterion 2 requirement; because thrust was not measured, Criterion 2 is analytically plausible but not experimentally closed. RPM, airspeed, neutral point, and aerodynamic derivatives were also not measured. The centreline propulsor cannot generate an independent pure roll moment. For small sideslip,

$$C_l \approx C_{l_\beta}\beta, \tag{10}$$

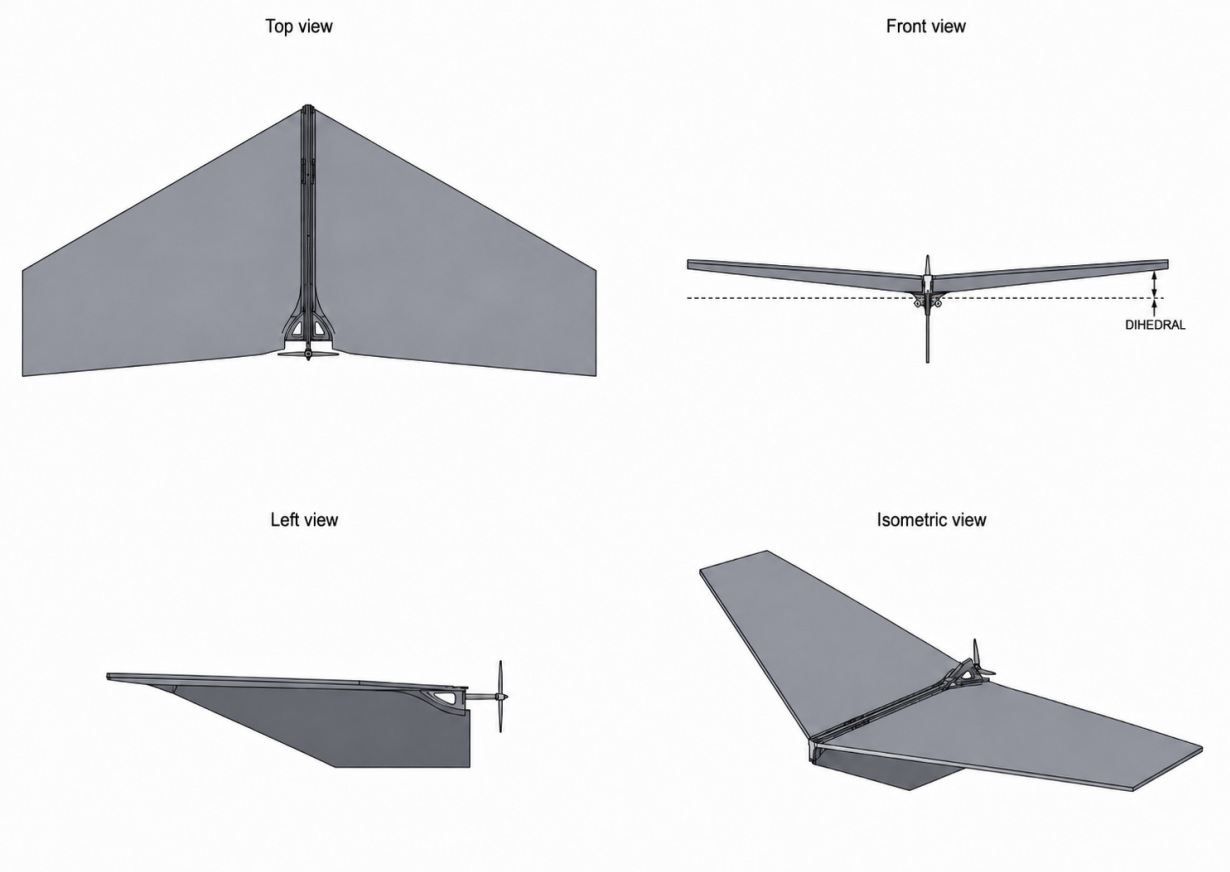


Figure 7 – Demonstrator drawing in top, front, left, and isometric views. The drawing defines the implemented airframe layout used in this paper; only the view titles and the dihedral annotation are retained because the remaining geometric quantities are stated directly in the text and Table 1.

and, after bank is established,

$$\dot{\psi} \approx \frac{g}{V} \tan \phi . \tag{11}$$

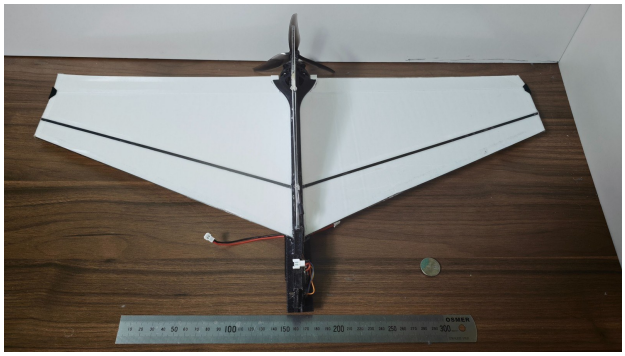
Classical tailless-aircraft analysis treats dihedral effect as a principal lateral-stability contribution [15]. NACA measurements quantify rolling moment due to sideslip for swept wings [16]. Standard lateral dynamics relate an established bank angle to turn rate [17]. On this basis, positive dihedral and sweep are intended to supply the required sign of coupling so that vector-induced yaw and sideslip produce bank. The flight evidence shows turning, but does not identify C_{l_β}, turn rate, bandwidth, or disturbance rejection.

6. Criterion 3: physical integration

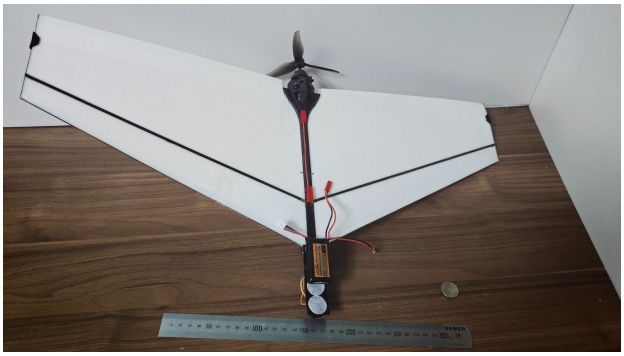
The propulsion-led method was implemented in a single-actuator fixed-wing demonstrator. Figure 7 defines the geometry: span $600\,\mathrm{mm}$, root chord $220\,\mathrm{mm}$, tip chord $100\,\mathrm{mm}$, leading-edge sweep about 25°, dihedral about 5°, and root incidence about 2.5°. The measured centre of gravity is $95\,\mathrm{mm}$ aft of the root leading edge. The wing-tip chord is parallel to the root chord, and a small centreline vertical stabilizer supplies directional support. The effective trailing-edge let-up was adjusted during flight preparation and is therefore a trim setting, not a fixed nominal geometric constant.

The measured mass breakdown is summarized in Table 1. The forward module is a battery/payload bay, the central wing is passive, and the rear module contains the ESC, controller, receiver, rotary encoder, BLDC motor, RES shaft, and propeller. The installed aircraft has one primary moving propulsion/control assembly and no wing-mounted servos, pushrods, control horns, or hinged trailing-edge surfaces. This is an architectural count; assembly time, cost, reliability, and mass benefit have not been measured against a matched conventional aircraft.

The rear centreline propeller is approximately $25\,\mathrm{mm}$ aft of the root trailing-edge point. It is a three-blade $5.1\,\mathrm{in}$ unit with approximately $4.66\,\mathrm{in}$ pitch. Thrust-line placement remains part of the control



(a) Assembled demonstrator without battery installed.



(b) Assembled demonstrator with battery installed for flight configuration.

Figure 8 – Photographs of the implemented prototype airframe. View (a) shows the flown single-actuator platform in planform, illustrating the tailless wing, centreline vertical stabilizer, and rear pusher installation. View (b) shows the same prototype with battery installed, making the forward payload bay and practical flight-ready configuration visible. The ruler and coin are included only as informal scale references.

Table 1 – Measured configuration quantities for the flown demonstrator.

Quantity	**Value**
Total mass	109.8 g
Battery mass	31.4 g
Propeller + RES mass	6.1 g
Motor + avionics mass	21.6 g
FPV camera mass	5.0 g
Remaining structure mass	45.7 g
Measured CG location	95 mm aft of root leading edge
Installed moving assemblies	1 primary propulsion/control assembly

architecture because

$$\mathbf{M}_T = \mathbf{r}_T \times \mathbf{T}, \tag{12}$$

and powered trim requires

$$\mathbf{M}_{\text{trim}} = \mathbf{r}_T \times \mathbf{T} + \mathbf{M}_{\text{react}} + \mathbf{M}_{\text{aero}} \approx \mathbf{0}. \tag{13}$$

The neutral propulsor is slightly below the aircraft reference line and passes close to, but below, the centre of gravity. Empirical installation biases are 0.5°–1° right yaw and about 5° downward pitch. Propeller reaction, aerodynamic trim moment, and thrust-line moment were not independently measured, so no causal decomposition is claimed. Criterion 3 is met as physical integration, not as a demonstrated cost, mass, or durability advantage.

7. Criterion 4: controlled flight

The evidence set contains Flight 1 View A [22] and Flight 2 Views A and B [23]. The three recordings therefore document two separate flights: Flight 1 is approximately 1 min and Flight 2 is approximately 3 min, with the latter recorded from two viewpoints. Across these flights, the recordings show hand launch, sustained forward flight, straight departure and approach, and repeated turning. These are demonstrated flight-recording durations, not measurements of maximum endurance.

The pilot interface is a 3-DoF command set comprising throttle, pitch, and roll. Throttle sets flight energy and available vector authority; pitch commands the longitudinal vector component; and the nominal roll command produces a lateral vector component whose yaw/sideslip response is converted into bank by the swept, dihedral wing. The recordings support practical controllability of this configuration at proof-of-concept level. They do not provide synchronized command histories, bank angle, turn rate, airspeed, rise time, or disturbance-rejection margins.



(a) Departure into sustained forward flight.

(b) Straight approach flight.

(c) Representative turning flight.

Figure 9 – Representative still frames extracted from the prototype flight-video set. The frames show proof-of-concept states corresponding to departure into sustained forward flight, straight approach flight, and a representative turning condition.

Representative frames in Fig. 9 show the three qualitative states used for Criterion 4. They make the flight evidence visible in the paper but do not replace calibrated state histories.

8. Evidence audit and validation route

The following audit closes the four-criterion argument while keeping each supported result beside its evidence status and boundary.

Criterion 1: vector generation. The physical result is a $10^\circ \pm 1^\circ$ optically estimated half-angle with full 360° azimuth; values up to about 15° were observed only nearer resonance. Bandwidth, phase lag, load dependence, efficiency, repeatability, and fatigue are not established.

Criterion 2: aircraft-level authority. The measured arm is $l = 162 \pm 1\,\mathrm{mm}$; the estimated restoring moment is 0.0045–$0.0054\,\mathrm{N\,m}$; and the corresponding thrust requirement is 0.160–$0.192\,\mathrm{N}$. This is an analytical requirement, and the experimental pass remains open because thrust, RPM, airspeed, aerodynamic derivatives, and lateral authority were not measured.

Criterion 3: physical integration. The measured aircraft mass is $109.8\,\mathrm{g}$, with one propulsion/control assembly and no wing-mounted actuators. The configuration is measured, but matched mass, cost, assembly-time, reliability, and durability benefits are not established.

Criterion 4: controlled flight. Three recordings from two flights show launch, straight flight, and turning. The flights are approximately $1\,\mathrm{min}$ and $3\,\mathrm{min}$ in the available recordings; these durations do not establish maximum endurance. State histories, command response, system identification, and repeatability statistics are not established.

The minimum next campaign is correspondingly specific: (1) measure thrust, RPM, torque modulation, $\delta(t)$, and $\chi(t)$ at the approximately 70% reference condition; (2) sweep frequency below and above resonance to identify $G_{\delta\tau}$, phase lag, and bandwidth; (3) identify effective TPU stiffness and damping from bench data; (4) synchronize pilot commands, airspeed, attitude, and vector state over repeated manoeuvres; (5) repeat tests across RES geometry, thrust-line setting, and passive-stability level; and (6) compare mass, cost, assembly time, efficiency, and structural life with a matched conventional airframe. A calibrated RealFlight model may then support controlled parametric comparison, but simulator output alone remains non-physical evidence.

9. Conclusion

The literature review relates RES to morphing structures, compliant mechanisms, flexible-shaft dynamics, distributed propulsion, and modern UAV thrust vectoring while maintaining the distinction between those fields and the present architecture. The evidence then supports four bounded conclusions. Criterion 1: RES produces a repeatable $10^\circ \pm 1^\circ$ cruise-like vector half-angle with full azimuthal coverage. Criterion 2: for the stated aerodynamic assumptions, the measured $162 \pm 1\,\mathrm{mm}$ arm

and nominal vector angle would balance an estimated 0.0045–$0.0054\,\mathrm{N\,m}$ restoring moment at 0.160–$0.192\,\mathrm{N}$ thrust; measured thrust is still required to close this criterion experimentally. Criterion 3: the mechanism is integrated into a $109.8\,\mathrm{g}$ fixed-wing aircraft as one centreline propulsion/control assembly without wing-mounted actuators. Criterion 4: three recordings from two flights show launch, sustained forward flight, straight flight, and turning; the longer recorded flight is approximately $3\,\mathrm{min}$. These results establish feasibility of the integrated concept, not complete performance. The paper does not establish control bandwidth, calibrated flight dynamics, aerodynamic efficiency, cost reduction, structural-life advantage, maximum endurance, or superiority over a matched aircraft. The flexible-body model defines the rotor-axis variables and frequency-response path required for the next quantitative campaign, but raw histories and effective properties must be identified before geometric vector prediction.

10. Corresponding author and contact information

Correspondence concerning this paper should be addressed to Haofei Guan, The University of Sydney, hgua8006@uni.sydney.edu.au.
Co-author contact: KC Wong, The University of Sydney, kc.wong@sydney.edu.au.

11. Copyright Statement

The authors confirm that they, and/or their company or organization, hold copyright on all of the original material included in this paper. The authors also confirm that they have obtained permission, from the copyright holder of any third party material included in this paper, to publish it as part of their paper. The authors confirm that they give permission, or have obtained permission from the copyright holder of this paper, for the publication and distribution of this paper as part of the ICAS proceedings or as individual off-prints from the proceedings.

Paper ID: ICAS2026_0484.
Proposed proceedings DOI form: 10.71945/icas2026_0484.

References

[1] Barbarino S, Bilgen O, Ajaj RM, Friswell MI, Inman DJ. A review of morphing aircraft. *Journal of Intelligent Material Systems and Structures*. 2011;22(9):823–877. doi:10.1177/1045389X11414084.

[2] Chu L, Li Q, Gu F, Du X, He Y, Deng Y. Design, modeling, and control of morphing aircraft: a review. *Chinese Journal of Aeronautics*. 2022;35(5):220–246. doi:10.1016/j.cja.2021.09.013.

[3] Osborn R, Kota S, Ervin G, Youngren H, Flick P. Mission Adaptive Compliant Wing: design, performance and flight test results. *50th AIAA/ASME/ASCE/AHS/ASC Structures, Structural Dynamics, and Materials Conference*, AIAA 2009-2126, 2009. doi:10.2514/6.2009-2126.

[4] Zhang Y, Ge W, Zhang Z, Mo X, Zhang Y. Design of compliant mechanism-based variable camber morphing wing with nonlinear large deformation. *International Journal of Advanced Robotic Systems*. 2019;16(6). doi:10.1177/1729881419886740.

[5] Mohiuddin MA, Khulief YA. Coupled bending torsional vibration of rotors using finite element. *Journal of Sound and Vibration*. 1999;223(2):297–316. doi:10.1006/jsvi.1998.2095.

[6] Al-Bedoor BO. Dynamic model of coupled shaft torsional and blade bending deformations in rotors. *Computer Methods in Applied Mechanics and Engineering*. 1999;169(1–2):177–190. doi:10.1016/S0045-7825(98)00184-4.

[7] Borer NK, Patterson MD, Viken JK, Moore MD, Bevirt J, Stoll AM, Gibson AR. Design and performance of the NASA SCEPTOR distributed electric propulsion flight demonstrator. *16th AIAA Aviation Technology, Integration, and Operations Conference*, AIAA 2016-3920, 2016. doi:10.2514/6.2016-3920.

[8] Kim HD, Perry AT, Ansell PJ. A review of distributed electric propulsion concepts for air vehicle technology. *2018 AIAA/IEEE Electric Aircraft Technologies Symposium*, AIAA 2018-4998, 2018. doi:10.2514/6.2018-4998.

[9] Erhard RM, Clarke MA, Alonso JJ. A low-cost aero-propulsive analysis of distributed electric propulsion aircraft. *AIAA SciTech 2021 Forum*, AIAA 2021-1200, 2021. doi:10.2514/6.2021-1200.

[10] Ryll M, Bülthoff HH, Giordano PR. A novel overactuated quadrotor unmanned aerial vehicle: modeling, control, and experimental validation. *IEEE Transactions on Control Systems Technology*. 2015;23(2):540–556. doi:10.1109/TCST.2014.2330999.

[11] Oosedo A, Abiko S, Narasaki S, Kuno A, Konno A, Uchiyama M. Flight control systems of a quad tilt rotor unmanned aerial vehicle for a large attitude change. *2015 IEEE International Conference on Robotics and Automation*, pp. 2326–2331, 2015. doi:10.1109/ICRA.2015.7139508.

[12] Invernizzi D, Lovera M. Trajectory tracking control of thrust-vectoring UAVs. *Automatica*. 2018;95:180–186. doi:10.1016/j.automatica.2018.05.024.

[13] Welstead J, Crouse GL Jr. Conceptual design optimization of an augmented stability aircraft incorporating dynamic response and actuator constraints. *52nd Aerospace Sciences Meeting*, AIAA 2014-0187, 2014. doi:10.2514/6.2014-0187.

[14] Ananda GK, Deters RW, Selig MS. *Propeller Induced Flow Effects on Wings at Low Reynolds Numbers*. AIAA 2013-3193, 31st AIAA Applied Aerodynamics Conference, 2013. URL: https://m-selig.ae.illinois.edu/pubs/AnandaDetersSelig-2013-AIAA-2013-3193-PropSlipstream.pdf.

[15] Donlan CJ. *An Interim Report on the Stability and Control of Tailless Airplanes*. NACA Report 796, 1944. URL: https://ntrs.nasa.gov/api/citations/19930091873/downloads/19930091873.pdf.

[16] Polhamus EC, Sleeman WC Jr. *The Rolling Moment Due to Sideslip of Swept Wings at Subsonic and Transonic Speeds*. NACA Research Memorandum L54L01, 1955. URL: https://ntrs.nasa.gov/api/citations/19930088609/downloads/19930088609.pdf.

[17] MIT OpenCourseWare. *Aircraft Lateral Dynamics: Spiral, Roll, and Dutch Roll Modes*. 16.333 Aircraft Stability and Control, Lecture 8, 2004. URL: https://ocw.mit.edu/courses/16-333-aircraft-stability-and-control-fall-2004/cd0b5972e3e365a692ca1de99d30bcb8_lecture_8.pdf.

[18] Spencer B Jr. *A Simplified Method for Estimating Subsonic Lift-Curve Slope at Low Angles of Attack for Irregular Planform Wings*. NASA Technical Memorandum X-525, 1961. URL: https://ntrs.nasa.gov/api/citations/19650072761/downloads/19650072761.pdf.

[19] The MathWorks, Inc. *Frequency Response Estimator and sinestream frequency-response estimation*. Documentation accessed 2026-07-31. URL: https://www.mathworks.com/help/slcontrol/ug/frequencyresponseestimator.html.

[20] Guan H, Wong KC. Spring-Damped Underactuated Swashplateless Rotor on a Bicopter Unmanned Aerial Vehicle. *Machines*. 2024;12(5):296. doi:10.3390/machines12050296.

[21] Guan H. Swashplateless underactuated rotor - drive-vector interpretation algorithm (test video). *YouTube video*, 2024. Accessed: 2026-01-03. URL: https://youtu.be/MSakM1UYp4I.

[22] Guan H. Prototype flight demonstration of the single-actuator RES fixed-wing demonstrator, view 1. *YouTube video*, flight evidence cited in this paper. URL: https://youtu.be/-65fTmqnwfc.

[23] Guan H. Prototype flight demonstration of the single-actuator RES fixed-wing demonstrator, view 2. *YouTube video*, flight evidence cited in this paper. URL: https://youtu.be/CrT-M2NsSh0.